A&A 603, A93 (2017)
DOI: 10.1051/0004-6361/201731037

Astronomy & Astrophysics

Dust and gas in star-forming galaxies at $z \sim 3$

Extending galaxy uniformity to 11.5 billion years⋆

G. E. Magdis[1,2], D. Rigopoulou[3,4], E. Daddi[5], M. Bethermin[6], C. Feruglio[7], M. Sargent[8], H. Dannerbauer[9,10], M. Dickinson[11], D. Elbaz[5], C. Gomez Guijarro[1], J.-S. Huang[12,13,14], S. Toft[1], and F. Valentino[1]

[1] Dark Cosmology Centre, Niels Bohr Institute, University of Copenhagen, Juliane Mariesvej 30, 2100 Copenhagen, Denmark
e-mail: magdis@dark-cosmology.dk
[2] Institute for Astronomy, Astrophysics, Space Applications and Remote Sensing, National Observatory of Athens, 15236 Athens, Greece
[3] Department of Physics, University of Oxford, Keble Road, Oxford OX1 3RH, UK
[4] Space Science & Technology Department, Rutherford Appleton Laboratory, Chilton, Didcot, Oxfordshire OX11 0QX, UK
[5] CEA, Laboratoire AIM, Irfu/SAp, 91191 Gif-sur-Yvette, France
[6] Aix-Marseille Univ., CNRS, LAM, Laboratoire d'Astrophysique de Marseille, 13013 Marseille, France
[7] INAF Observatory of Trieste, via G. B. Tiepolo 11, 34143 Trieste, Italy
[8] Astronomy Centre, Department of Physics and Astronomy, University of Sussex, Falmer, Brighton BN1 9QH, UK
[9] Instituto de Astrofisica de Canarias (IAC), 38205 La Laguna, Tenerife, Spain
[10] Universidad de La Laguna, Dpto. Astrofisica, 38206 La Laguna, Tenerife, Spain
[11] NOAO, 950 N. Cherry Avenue, Tucson, AZ 85719, USA
[12] National Astronomical Observatories of China, Chinese Academy of Sciences, 100012 Beijing, PR China
[13] China-Chile Joint Center for Astronomy, Chinese Academy of Sciences, Camino El Observatorio, 1515 Las Condes, Santiago, Chile
[14] Harvard-Smithsonian Center for Astrophysics, 60 Garden Street, Cambridge, MA 02138, USA

Received 25 April 2017 / Accepted 15 May 2017

ABSTRACT

We present millimetre dust emission measurements of two Lyman-break galaxies at $z \sim 3$ and construct for the first time fully sampled infrared spectral energy distributions (SEDs), from mid-IR to the Rayleigh-Jeans tail, of individually detected, unlensed, UV-selected, main sequence (MS) galaxies at $z = 3$. The SED modelling of the two sources confirms previous findings, based on stacked ensembles, of an increasing mean radiation field $\langle U \rangle$ with redshift, consistent with a rapidly decreasing gas metallicity in $z > 2$ galaxies. Complementing our study with CO[$J = 3 \rightarrow 2$] emission line observations, we have measured the molecular gas mass reservoir ($M_{\rm H_2}$) of the systems using three independent approaches: 1) CO line observations; 2) the dust to gas mass ratio vs. metallicity relation; and 3) a single band, dust emission flux on the Rayleigh-Jeans side of the SED. All techniques return consistent $M_{\rm H_2}$ estimates within a factor of two or less, yielding gas depletion time-scales ($\tau_{\rm dep} \approx 0.35$ Gyr) and gas-to-stellar mass ratios ($M_{\rm H_2}/M_* \approx 0.5{-}1$) for our $z \sim 3$ massive MS galaxies. The overall properties of our galaxies are consistent with trends and relations established at lower redshifts, extending the apparent uniformity of star-forming galaxies over the last 11.5 billion years.

Key words. evolution – infrared: galaxies – galaxies: high-redshift – galaxies: evolution – galaxies: ISM

1. Introduction

Star formation in galaxies proceeds through the conversion of molecular hydrogen into stars, in dense molecular clouds (e.g., Fukui & Kawamura 2010). It naturally follows that any attempt to understand galaxy evolution and characterise the star formation history of the Universe requires the measurement of the molecular hydrogen mass reservoir ($M_{\rm H_2}$) of galaxies across cosmic time. To this end, several techniques that convert direct observables, or well calibrated derived quantities, to $M_{\rm H_2}$, have been developed and successfully applied. Applying these techniques to galaxy populations that meet various selection criteria and lie at different cosmic epochs, has revealed a consistent picture in which the star formation rate (SFR) and the molecular gas mass of the majority of star-forming galaxies at any redshift, are tightly correlated, following the so-called Schmidt-Kennicutt relation. This, along with the discovery of the main sequence (MS) of star formation approximately a decade ago (e.g. Noeske et al. 2007; Elbaz et al. 2007; Magdis et al. 2010a), provide evidence of a uniformity in the star formation histories and the star formation activity of the galaxies at least up to $z \approx 2$ (e.g. Daddi et al. 2010a,b; Magdis et al. 2012b; Sargent et al. 2014; Genzel et al. 2015; Tacconi et al. 2017).

Measuring $M_{\rm H_2}$ in galaxies though, becomes progressively more difficult and more demanding, in terms of required observational time per object, with look-back time. For example, CO lines, that are the most traditional gas mass tracer, have only been measured in a very small fraction of spectroscopically confirmed $z > 1$ galaxies (e.g. Solomon & Vanden Bout 2005; Carilli & Walter 2013; Bothwell et al. 2013; Aravena et al. 2016; Silverman et al. 2015; Tacconi et al. 2017), while at

⋆ *Herschel* is an ESA space observatory with science instruments provided by European-led Principal Investigator consortia and with important participation from NASA.

$z > 2.5$ are primarily restricted to lensed objects or strong starbursts (e.g. Saintonge et al. 2013; Dessauges-Zavadsky et al. 2015). Similarly, the dust to gas mass technique ($\delta_{\rm GD}$), that has become increasingly popular at high-z thanks to the advent of the *Herschel* Space Observatory (*Herschel*), requires detailed sampling of the far-IR spectral energy distribution (SED) and of the Rayleigh-Jeans (R-J) tail of the SED, and therefore is primarily restricted to $z < 2$ or extremely bright and rare sources at higher redshifts, due to the limited sensitivity of *Herschel*. Thus, the gas fraction and star formation efficiency of "normal" (MS) galaxies remain poorly constrained at $z > 2$.

In an attempt to extend $M_{\rm H_2}$ studies of normal galaxies to higher redshifts, Béthermin et al. (2015), applied the $\delta_{\rm GD}$ method in stacked ensembles of galaxies up to $z = 4$ (see also Santini et al. 2014; Genzel et al. 2015; Tacconi et al. 2017). Also, Scoville et al. (2017) and Schinnerer et al. (2016), were able to place constraints on the gas masses of individual galaxies up to $z = 4$, using single band measurements of the dust emission flux on the Rayleigh-Jeans side of their SED. Finally, Magdis et al. (2012a), and Tan et al. (2014), presented CO observations, and therefore $M_{\rm H_2}$ estimates for a two of $z = 3$–4 Lyman-break galaxies (LBGs). Clearly, we need a larger sample of high-z "normal" galaxies for which more than one method to derive $M_{\rm H_2}$ estimates can be applied, in order to increase the currently limited number of $z > 2.5$ galaxies with measured $M_{\rm H_2}$ but also check against systematics in $M_{\rm H_2}$ estimates among the various methods.

In this paper we combine mid to far-IR data with millimeter observations of the R-J tail and CO[$J = 3 \rightarrow 2$] emission line detections of two $z \sim 3$, UV selected, LBGs that lie on the MS of star formation, in order to 1) study their far-IR properties; 2) derive gas mass estimates using three independent techniques and 3) investigate the gas depletion time scales and gas fraction of individual MS galaxies at $z = 3$. Throughout the paper we refer to the molecular hydrogen gas mass as $M_{\rm H_2}$ and to the total gas mass, which is the sum of $M_{\rm H_2}$ and of the atomic gas mass ($M_{\rm HI}$), as $M_{\rm gas}$. We adopt $\Omega_{\rm m} = 0.3$, $H_0 = 71$ km s^{-1} Mpc^{-1}, $\Omega_\Lambda = 0.7$ and a Chabrier IMF (Chabrier 2003).

2. Sample and observations

2.1. Optical to mid-IR data

The two galaxies of this study, D49 (RA: 214.37169, Dec: +52.576303) and M28 (RA: 214.44282, Dec: +52.45561), were drawn from the optically selected (U, G, R) sample of $z \sim 3$ LBGs by Steidel et al. (2003) in the extended groth strip (EGS) field. Their selection was based on the available spectroscopic redshift ($z = 2.808$ and $z = 2.903$) determined by Ly-α emission through ground based rest-frame UV spectroscopy (Steidel et al. 2003; Shapley et al. 2003). Since the galaxies were selected for CO and dust continuum follow-up observations, a second criterion was a detection at 24 μm to ensure sufficiently high total infrared luminosities ($L_{\rm IR} > 10^{12}\,L_\odot$) that would make the detection experiment possible (Rigopoulou et al. 2010; Magdis et al. 2010b). This criterion biases our sample to the most massive and infrared luminous LBGs at $z \sim 3$ (e.g. Rigopoulou et al. 2006; Magdis et al. 2010b), which however have overall properties (in terms of specific SFR and star formation efficiency) similar to that of MS galaxies (see Sects. 3 and 4). Our sources benefit from extensive multi-wavelength coverage (Rigopoulou et al. 2006) including ground based (U, G, R, J, K, z) observations and photometry from the Advanced Camera for Surveys (ACS, *F606W* (V), *F814W* (i)), Infrared Array Camera (IRAC), and the Multi-band Imaging Photometer (MIPS) on board the *Spitzer* Space Telescope (*Spitzer*).

2.2. Herschel data

The EGS field has been observed by *Herschel* as part of the PACS evolutionary probe (PEP; Lutz et al. 2011) and the *Herschel* Multi-tiered Extragalactic Survey (HerMES, Oliver et al. 2010, 2012), providing 100 and 160 μm imaging with the Photodetector Array Camera and Spectrometer (PACS; Poglitsch et al. 2010) and 250, 350, and 500 μm with the Spectral and Photometric Imaging Receiver (SPIRE; Griffin et al. 2010), respectively. Since both our sources are detected at 24 μm, we performed *Herschel* photometry by using the source extraction point-spread function fitting code *Galfit* (Peng et al. 2002), guided by 24 μm priors. As a sanity check, we also compared the derived fluxes of our sources with those reported in the photometric catalogues provided by the PEP and HerMES teams. The catalogues were also produced based on a 24 μm prior source extraction technique. The derived fluxes between the various catalogues are in excellent agreement yielding a signal-to-noise ratio $S/N > 3$ detection of D49 in all 5 *Herschel* bands and of M28 at 250- and 350 μm. The derived *Herschel* fluxes for the two sources are summarised in Table 1.

2.3. Millimetre observations

The 1.2 mm continuum observations presented here were carried out during December 2005 and February 2006 using the 117-channel Max-Planck Millimetre Bolometer (MAMBO-2, Kreysa et al. 1999) array at the Institut de Radioastronomie Millimetrique (IRAM) 30 m telescope on Pico Veleta (Spain). MAMBO-2 operated at an effective wavelength of 1.2 mm which corresponds to 250 GHz ($FWHM \sim 10\farcs7$). The sources were observed with the array's central channel, using the standard on-off mode with the telescope secondary chopping in azimuth by 50″ at a rate of 2 Hz. The target was always positioned on the central bolometer of the array and after 10 s of integration the telescope was nodded so that the off-beam became the on-beam. On-off observations were obtained in 20 min scans with a wobbler throw of 35″ and were repeated until either a detection ($S/N \geq 3$) or a noise level of ~0.4 mJy was reached. Pointing was checked frequently on nearby continuum sources, and was found on average stable to 2″. Sky opacity was monitored regularly with zenith opacities at 1.2 mm and was found to vary between 0.06 and 0.4. Primary pointing, focus and flux calibrations were performed using observations of Mars (~130 mJy) or CW-LEO (~1.3 mJy).

The data were analysed using MOPSIC, an updated version of the MOPSI software developed by R. Zylka. Every scan and its associated sub-scans were carefully inspected for outliers or influence of high opacity – affected sub-scans were subsequently excluded from further reduction. Correlated sky-noise was computed for each channel separately as a weighted mean of the signals from the surrounding channels. Then the mean was subtracted from each channel. Both sources are detected at $S/N > 3$, with $S_{1.2\ \rm mm} = 1.76 \pm 0.37$ mJy for D49 and $S_{1.2\ \rm mm} = 1.10 \pm 0.36$ mJy (Table 1).

2.4. PdBI observations of D49

We targeted the CO[$J = 3 \rightarrow 2$] ($\nu_{\rm rest} = 345.796$ GHz) transition towards D49, using the Plateau de Bure Interferometer. At $z = 2.808$ this line is redshifted to 90.8078 GHz. Observations were

Table 1. Mid to far-IR and mm photometry.

Name	z_{spec}	S_{24} [mJy]	S_{100} [mJy]	S_{160} [mJy]	S_{250} [mJy]	S_{350} [mJy]	S_{500} [mJy]	$S_{1.2}$ [mJy]
D49	2.846	0.09 ± 0.03	4.27 ± 1.22	12.21 ± 3.56	15.08 ± 1.80	18.19 ± 1.84	11.83 ± 2.37	1.79 ± 0.37
M28	2.908	0.18 ± 0.02	2.05 ± 1.27	4.33 ± 2.8	10.12 ± 2.21	13.75 ± 1.87	5.32 ± 2.19	1.10 ± 0.36

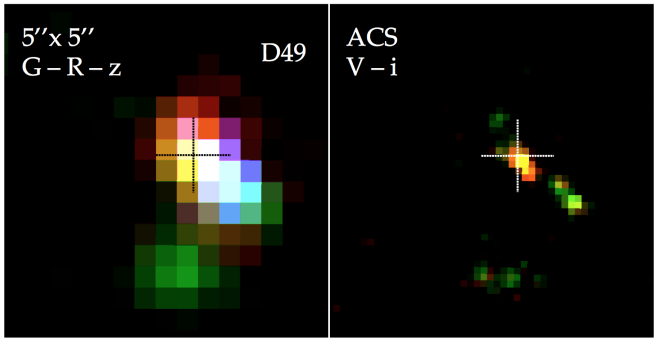

Fig. 1. *Left*: $G-R-z$, three colour image of D49, as obtained by ground based imaging. There is a clear colour gradient with CO emission centered at the position of the red component. *Right*: $V-i$, high-resolution two colour image obtained by ACS/HST. The system is resolved into two components (a red and a blue), separated by ∼1″. The cross (and its size) in each panel depicts the centroid (and the position uncertainty) of the line emission detected by PdBI.

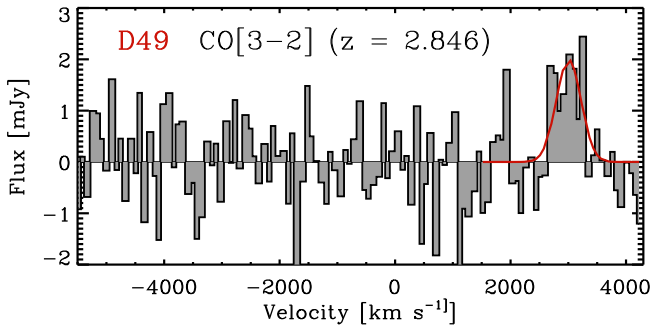

Fig. 2. Spectrum of CO[$J = 3 \rightarrow 2$] emission of D49, binned in steps of 65 km s^{-1}. The detected line is offset by ∼3000 km s^{-1}, with respect to the central frequency expected based on the redshift of the source obtained by Steidel et al. (2003). The red line corresponds to the gaussian fit to the detected line profile.

carried out under excellent 3 mm weather conditions in D array configuration with five and six antennas for 2.77 and 1.85 h respectively, in June 2014. Data reduction was performed using CLIC in GILDAS. The noise level reach by the combined observations is 0.29 mJy/beam in 128 MHz channels (∼ 400 km s^{-1}) and the full width at half maximum (FWHM) of the circularised synthesised beam is about 6″. We note that CO observations of M28 were not carried out.

We searched for CO emission at the optical position of the LBG (RA: 214.37169, Dec: +52.576303) and detected an emission line at $S/N = 5.8$ (Fig. 2). The spatial position of the peak line emission (RA: 214.37181, Dec: +52.576236 ± 0.6″) is consistent with the optical counterpart within the uncertainties but the detected line is redshifted ∼3000 km s^{-1} with respect to the expected frequency based on the optical redshift of the source. The fact that Ly-α is blueshifted rather than redshifted with respect to CO, does not support the scenario where the discrepancy originates from an extinction truncated Ly-α profile. Also, the scenario of outflows due to the presence of a strong AGN is disfavoured by the absence of strong AGN activity, advocated by the rest-frame UV spectrum, the lack of detection in the X-rays and the IRAC colours (e.g. Donley et al. 2012). On the other hand, a possible solution is that that the Ly-α and the 3 mm emission line are arising from two different but nearby systems; a dust obscured one and relatively dust free Ly-α emitting component.

This is supported from the three-colour image (GRz) shown in (Fig. 1 left), that reveals a colour gradient within the single source detected by ground based imaging. Upon inspection of the ACS images, that were not available in the original study of Steidel et al. (2003), it becomes evident that the single source seen in the ground based imaging is deblended into two components. Again, from the two colour ACS image ($V-i$, Fig. 1 right) it is clear that the system originally selected as a single LBG, consists of two components, a blue and a red that are ∼1″ apart. We note that the IRAC, MIPS 24 μm as well as the line emission are centered at the position of the red component. Assuming that the detected line is CO[$J = 3 \rightarrow 2$], the observed central frequency yields are redshift of $z = 2.846$ for the red component. Using the ACS photometry, and $\lambda > 6000$ Å ground based photometry (where the bulk of the emission is originating from the red component), we run the Le-Phare and Hyper-z phot-z codes to infer a photometric redshift for the red component. Both codes return a photo-z of 2.95 ± 0.22. Similarly the mid-IR to mm SED is consistent with a galaxy at $z \sim 3$ (see Sect. 4). An alternative scenario where the detected line is CO[$J = 4 \rightarrow 5$] of a $z = 4.11$ source, can be ruled out from the photo-z analysis as well as from the shape of the infrared SED. We conclude that detected line is CO[$J = 3 \rightarrow 2$], originating from the red component that lies at $z_{CO} = 2.846 \pm 0.011$, and which is responsible for the bulk of the near-IR to mm emission. We note that the CO redshift is inconsistent by more than 3σ with respect to the optical redshift derived by fitting the Ly-α emission line from the UV spectrum ($z_{opt} = 2.8079 \pm 0.0003$). Finally, we stress that whether this a single system consisting of two nearby galaxies lying 8 kpc apart (as indicated by their angular distance) and moving with 3000 km s^{-1} with respect to each other, or whether the two sources lie ∼40 Mpc apart (as indicated by their redshifts described above), does not change the results presented in this paper, as the bulk of CO, dust and stellar (>90%) emission originates from the red component.

3. Results

3.1. Far-IR properties

The far-IR properties of $z \sim 3$ LBGs have been investigated in previous studies (e.g. Magdis et al. 2010b, 2012a; Rigopoulou et al. 2010; Coppin et al. 2015). However, the majority of these studies are based on stacking results or on sparse sampling of the full IR SED. Here, we present and model mid-IR to mm SEDs of individually detected LBGs, with detailed coverage of the peak and the R-J part of the spectrum (Fig. 3).

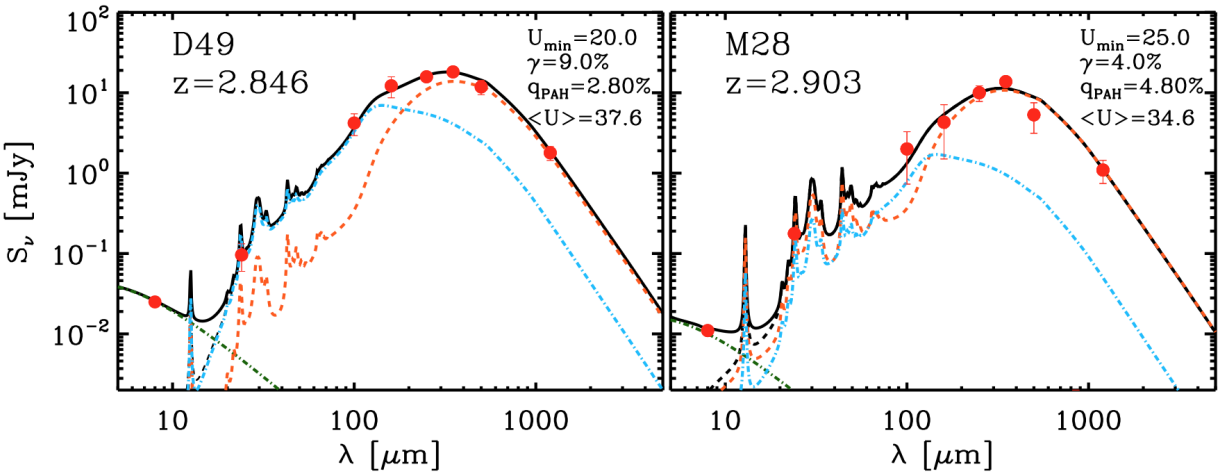

Fig. 3. Spectral energy distributions (observed frame) of D49 and M28, including IRAC 8 μm, MIPS 24 μm PACS 100, 160 μm and SPIRE 250, 350, and 500 μm and MAMBO 1.2 mm data points (red dots). The observed data are overlaid with the best-fit DL07 model (black line). The "PDR" and diffuse ISM components are shown in cyan and orange, respectively, while the stellar component is depicted with a green dashed-dotted line. On the top right of each panel we list the derived parameters from the SED modeling, including $U_{\rm min}$ (radiation field of the diffuse ISM), γ (the contribution of the PDR component in the total SED), $q_{\rm PAH}$ (the fraction of dust in PAHs) and $\langle U \rangle$ (mean radiation field).

We combine *Spitzer* IRAC (8.0 μm), MIPS (24 μm), *Herschel* PACS/SPIRE (100, 160 250, 350, and 500 μm) with the 1.2 mm IRAM continuum measurements and use the Draine & Li (2007, hereafter DL07) model to derive dust masses and infrared luminosities by fitting the mid-IR to sub-millimeter photometry. The analysis is also supplemented by a more simplistic but widely used single temperature modified blackbody (MBB) fit in order to derive a representative single dust temperature $T_{\rm d}$ of the ISM. In particular, we adopt a fixed effective dust emissivity index of $\beta = 1.8$ and fit observed data points with $\lambda_{\rm rest} > 50\,\mu$m to avoid emission from very small grains that dominate at shorter wavelengths. A similar technique for the derivation of $M_{\rm dust}$, $T_{\rm d}$, and $L_{\rm IR}$ using the DL07 and MBB models is presented in detail in Magdis et al. (2012b, 2013). The best-fit model SEDs are presented in Fig. 3. The derived luminosities and dust masses are, $L_{\rm IR} = (6.02 \pm 0.41) \times 10^{12}\,L_{\odot}$ and $M_{\rm dust} = (1.34 \pm 0.36) \times 10^{9}\,M_{\odot}$ for D49 and $L_{\rm IR} = (3.16 \pm 0.29) \times 10^{12}\,L_{\odot}$ and $M_{\rm dust} = (7.95 \pm 2.74) \times 10^{8}\,M_{\odot}$ for M28. Similarly, the corresponding dust temperatures obtained from the MBB model are 41 ± 2 K and 41.8 ± 3 K for D49 and M28 respectively. The derived far-IR properties of the galaxies are summarised in Table 2.

3.2. CO emission properties

To measure the velocity centroid and line width of the CO emission from D49, we fit a single Gaussian to the observed spectrum (Fig. 2), extracted at the phase center, that coincides with the position of the red component seen in the optical band. The fit yields a peak flux density of $S_{\rm CO} = 1.99 \pm 0.12$ mJy, a FWHM of 501 ± 35 km s^{-1} and the velocity integrated flux is $I_{\rm CO} = 1.10 \pm 0.18$ Jy km s^{-1}. We derive the CO[$J = 3 \rightarrow 2$] line luminosity of D49 ($L_{\rm CO[3-2]}$, in K km s^{-1} pc^2), from the detected velocity integrated flux ($S_{\rm CO}\Delta u$) using the Eq. (3) in Solomon & Vanden Bout (2005):

$$L_{\rm CO[3-2]} = 3.25 \times 10^7\, S_{\rm CO}\Delta u\, \nu_{\rm obs}^{-2}\, D_{\rm L}^2\, (1+z)^{-3}, \quad (1)$$

where $S_{\rm CO}\Delta u$ is in Jy km s^{-1}, $\nu_{\rm obs}$ is the observed frequency of the detected line (CO[$J = 3 \rightarrow 2$]) in GHz, and $D_{\rm L}$ is the luminosity distance in Mpc. The inferred CO[$J = 3 \rightarrow 2$] luminosity is $L_{\rm CO[3-2]} = (4.16 \pm 0.68) \times 10^{10}$ K km s^{-1} pc^2.

3.3. Position relative to Main Sequence

To determine the position of the two galaxies with respect to the MS, we need to determine the SFRs and stellar masses. For the former, we convert the inferred IR luminosities to SFRs adopting the Kennicutt 1998 SFR to $L_{\rm IR}$ conversion for a Chabrier IMF. For the latter, we consider the available UV to near-IR photometry and use the BC03 models assuming a constant star formation history. Our analysis yields a SFR of 600 $M_{\odot}$ yr^{-1} and a stellar mass of $1.9 \times 10^{11}\,M_{\odot}$ for D49 while the corresponding values for M28 are $SFR = 320\,M_{\odot}$ yr^{-1} and $M_{*} = 2.4 \times 10^{11}\,M_{\odot}$. We note that the inferred stellar masses are in agreement with the values reported in Rigopoulou et al. (2006). In Fig. 4, we present the position of the two sources in the SFR-M_{*} plane along with the stellar mass and redshift dependent MS description of Schreiber et al. (2015) at $z = 3.0$. Despite their high $L_{\rm IR}$ both sources appear to have specific SFRs consistent with that of Main sequence galaxies at their corresponding redshift and are placed at the high-mass end of the relation, where there is recent evidence for a bending of the MS (e.g. Schreiber et al. 2015; Lee et al. 2015).

Finally, using the extinction values from the best fit BC03 models ($E(B-V) \approx 0.27$ for both sources) we derive UV dust-corrected SFRs ($SFR_{\rm UVcor}$) estimates, by converting the extinction-corrected UV-luminosity L_{1500} to SFR (Daddi et al. 2007; Magdis et al. 2010c). For D49, we find $SFR_{\rm UVcor} = 325\,M_{\odot}$ yr^{-1} and for M28, $SFR_{\rm UVcor} = 230\,M_{\odot}$ yr^{-1}. While these UV-based SFR estimates are ~1.5–2 times lower compared to the IR-based SFR, this discrepancy is considerably lower than what is found for local ULIRGs and high-z starbursts ($SFR_{\rm IR}/SFR_{\rm UVcor} \gg 3$), and closer to that found for normal galaxies (e.g., Elbaz et al. 2007; Magdis et al. 2010c; Rigopoulou et al. 2010).

4. Discussion

4.1. Evolution of the mean radiation field $\langle U \rangle$

The dust mass weighted luminosity of the galaxies ($M_{\rm dust}/L_{\rm IR}$), (proportional to the mean radiation field, $\langle U \rangle \propto M_{\rm dust}/L_{\rm IR}$) and its evolution with redshift, has been shown to trace the evolution of

Table 2. Physical properties.

Name	$\log L_{\rm IR}$ $[L_\odot]$	$I_{\rm CO[3-2]}$ [Jy km s^{-1}]	$L'_{\rm CO}{}^{a}$ [K km s^{-1} pc^2]	$\log M_{\rm dust}{}^{b}$ $[M_\odot]$	$\log M_{\rm H_2}{}^{c}$ $[M_\odot]$	$\log M_*$ $[M_\odot]$	$\langle U \rangle$ –	$T_{\rm d}{}^{d}$ [K]
D49	12.78 ± 0.03	1.10 ± 0.18	10.93 ± 0.11	9.12 ± 0.12	11.32 ± 0.15	11.28 ± 0.12	35.7 ± 7.0	40.6 ± 2.0
M28	12.51 ± 0.04	–	–	8.90 ± 0.15	11.01 ± 0.12	11.38 ± 0.10	32.2 ± 8.0	41.8 ± 3.0

Notes. [(a)] CO[1–0] luminosity assuming an excitation correction of $r_{31} = 0.5$. The quoted uncertainty includes the observed uncertainty in the flux measurement and the uncertainty in r_{31}, in quadrature. [(b)] Derived based on DL07 models. [(c)] Average value, between CO, $\delta_{\rm GD}$ and R-J approach. [(d)] Based on a MBB model with fixed $\beta = 1.8$.

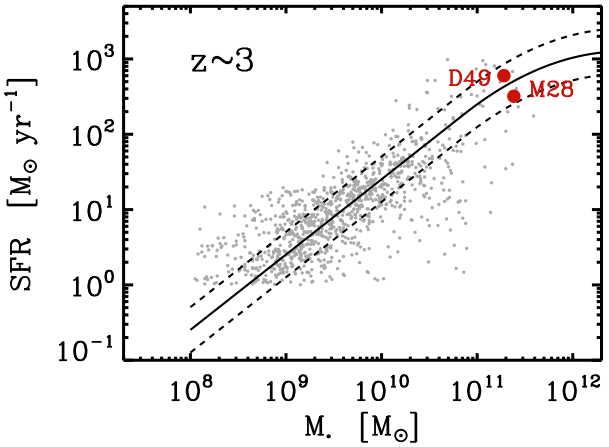

Fig. 4. Location of D49 and M28 (red circles) with respect to the main sequence at $z = 3$ (solid line) and its scatter (dashed lines), as measured by Schreiber et al. (2015). Grey circles correspond to $2.7 < z < 3.2$ galaxies in GOODS-S with measured SFR and M_*.

the shape of the far-IR SED, of the dust temperature of the ISM and more recently of the gas phase metallicity in MS galaxies along cosmic time. In particular, this quantity yields the emitted energy per unit dust mass, and for the case of a MBB with an effective dust emissivity index of β, it is related to $T_{\rm d}$ through the following formula:

$$\langle U \rangle \propto \frac{L_{\rm IR}}{M_{\rm dust}} \propto T_{\rm d}^{4+\beta}. \quad (2)$$

Using stacked ensembles of MS galaxies, Magdis et al. (2012b) and Béthermin et al. (2015), showed that for galaxies within the MS $\langle U \rangle$ increases with redshift as $(1+z)^{\zeta}$ (with ζ ranging between 1.2 and 1.8 among several studies) providing evidence of MS galaxies becoming warmer as we move back in time. A similar evolution of the $T_{\rm d}$ of MS galaxies with redshift has also been reported by Magnelli et al. (2014).

Furthermore, the evolution of $\langle U \rangle$ with redshift can be used to test various scenarios of the evolution of the gas-phase metallicity of the galaxies. In particular, it is still debated if the fundamental metallicity relation (FMR, Mannucci et al. 2010) that relates the gas phase metallicity to the M_* and the SFR of a star-forming galaxy, holds beyond $z = 2$, or whether it breaks down, with galaxies at higher-z having lower metallicities than those inferred by the FMR prescription. The latter is supported by various recent studies (e.g., Troncoso et al. 2014; Amorín et al. 2014; Steidel et al. 2014) including Onodera et al. (2016), who showed that the metallicity of $z \sim 3.0$ star-forming galaxies is offset by ~0.3 dex from the locally defined FMR relation. Their results are consistent with the redshift evolution of the mass-metallicity relation prescribed by Lilly et al. (2013).

In Magdis et al. (2012b) we showed that since $\langle U \rangle \propto L_{\rm IR}/M_{\rm dust}$, $M_{\rm dust} \propto M_{\rm gas} \times Z(M_*, SFR)$ (e.g., Leroy et al. 2011) and $L_{\rm IR} \propto SFR \propto M_{\rm gas}^{\gamma}$ (Kennicutt relation) then:

$$\langle U \rangle \propto \frac{L_{\rm IR}}{M_{\rm gas} \times Z} = \frac{SFR^{1-\gamma}}{Z(M_*, SFR)}. \quad (3)$$

Assuming $\gamma = 0.83$, as reported by Sargent et al. (2014), Béthermin et al. (2015), calculated the expected evolution of $\langle U \rangle$, for the following two evolutionary scenarios for the gas phase metallicity: 1) a redshift invariant FMR (universal FMR) and 2) an FMR relation with a correction of $0.30 \times (1.7 - z)$ dex (broken FMR), to account for the deviation between recent metallicity measurements of high-z galaxies and those prescribed by a universal FMR (see Tan et al. 2014). At fixed stellar mass, the first case predicts a smooth increase of $\langle U \rangle$ with redshift, depicting the decrease of Z as we move to higher-z, due to the increase of SFR with redshift along the MS. On the other hand, a broken FMR predicts a steep increase of $\langle U \rangle$ beyond $z > 1.7$. Comparing the two evolutionary tracks to the average $\langle U \rangle$ values of MS galaxies at different redshift bins as derived from stacking, they found that the observed evolution of $\langle U \rangle$, is consistent with the case of a broken FMR.

Here we can further inform and test the observed trends emerging from stacking results with direct measurements of $L_{\rm IR}$ and $M_{\rm dust}$ of individual MS galaxies at $z \sim 3$. In Fig. 5, we present the evolution of $\langle U \rangle$ with redshift as derived from stacking of MS galaxies at various redshift from Magdis et al. (2012b) and Béthermin et al. (2015), along with the direct measurements for our two galaxies. With $\langle U \rangle$ measurements of 35.7 ± 7.0 for D49 and 32.2 ± 8.0 for M28, the individual detections appear to be in excellent agreement with the average $\langle U \rangle$ at the corresponding redshift presented in Béthermin et al. (2015). Also, our measurements appear consistent with a broken FMR, lying ~2–3σ above the prediction of a universal FMR. Brought together our analysis, confirms the increase of $\langle U \rangle$ of MS galaxies at $z > 2$, and supports the scenario where the metallicity of $z > 2$ galaxies is better described by a broken FMR.

4.2. Molecular gas mass estimates

In recent years we have witnessed great progress in the determination of the gas mass reservoirs of galaxies across cosmic time. Such measurements are based either 1) on the more traditional conversion of the integrated CO line luminosity $L'_{\rm CO}$ to $M_{\rm H_2}$ using the $\alpha_{\rm CO}$ conversion factor; or 2) on the more recently introduced metallicity-dependent dust-to-gas mass ratio technique ($\delta_{\rm GD}$), that exploits the consistent derivation of $M_{\rm dust}$ allowed by detailed sampling of the far-IR SED by *Herschel* and other (sub)mm facilities or 3) on the single band measurement of the dust emission flux on the Rayleigh-Jeans side of the SED (e.g. Scoville et al. 2014; Groves et al. 2015; Schinnerer et al. 2016).

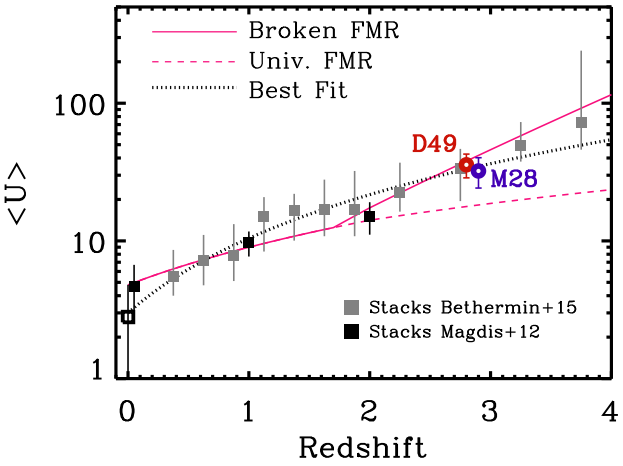

Fig. 5. Evolution of the mean radiation field, or equally, of the dust mass weighted luminosity, with redshift of main sequence galaxies. The red and blue circles correspond to the $\langle U \rangle$ values of D49 and M28 as derived from the DL07 models. The grey and black squares correspond to the average $\langle U \rangle$ values of MS galaxies as derived from the stacking analysis of Béthermin et al. (2015) and Magdis et al. (2012b) respectively. The open black square corresponds to the mean value of the local *Herschel* Reference Sample by Ciesla et al. (2014). The solid and dashed pink lines represent the evolutionary trends expected for a broken and universal FMR, respectively, while the dotted line depicts the best fit to the data.

With our data we are now able to compare measurements of M_{H_2} inferred using all three independent methods for the first time for $z = 3$ MS galaxies.

4.2.1. CO based M_{H_2}

The M_{H_2} of the galaxies is related to the CO[$J = 1 \rightarrow 0$] line luminosity (L'_{CO}) through the equation:

$$M_{H_2}\,[M_\odot] = \alpha_{CO} \times L'_{CO}, \quad (4)$$

where α_{CO} is the CO to M_{H_2} conversion factor.

Since our PdBI observation of D49 traces the CO[$J = 3 \rightarrow 2$] rather than the fundamental CO[$J = 1 \rightarrow 0$] emission line we need to adopt an excitation correction (r_{31}) to convert the observed $L_{CO[3-2]}$ to L'_{CO}. While, Carilli & Walter (2013) find that r_{31} can vary from 0.27 (Milky Way) to 0.97 (quasars), studies of typical star-forming galaxies and starburst galaxies find a fairly consistent average value of $\langle r_{31} \rangle \sim 0.42{-}0.65$ (Dannerbauer et al. 2009 ; Tacconi et al. 2010; Carilli & Walter 2013; Greve et al. 2014; Genzel et al. 2015; Daddi et al. 2015; Sharon et al. 2016). Here, we adopt the median value of $\langle r_{31} \rangle \sim 0.5$ reported in various studies, along with an uncertainty of 0.15, to account for the observed variations among various samples in the literature, and derive $L'_{CO} = (8.67 \pm 2.6) \times 10^{10}\,L_\odot$.

In addition to the adopted r_{31}, a further assumption needs to be made regarding the choice of the value of α_{CO}, that is known to vary as a function of metallicity and possibly depends on the star formation mode of the galaxy. Since we lack direct measurements of the gas-phase metallicity for D49, we choose to adopt a solar metallicity that is very close to the average value between the cases of a broken and universal FMR discussed above. Subsequently, we use various $\alpha_{CO} - Z$ relations reported in the literature (Leroy et al. 2011; Magdis et al. 2012b; Genzel et al. 2012) and derive an average $\alpha_{CO} = 3.5$, which is a typical value for MS galaxies at various redshifts. Under these assumptions and combining all uncertainties in quadrature we derive $\log(M_{H_2}\,[M_\odot]) = 11.48 \pm 0.23$.

4.2.2. δ_{GD} based M_{H_2}

This method and its associated uncertainties have been presented in detail in various studies (e.g., Magdis et al. 2011, 2012b; Berta et al. 2016). In brief, if the metallicity and the M_{dust} of a galaxy are known, then one can use the well calibrated local M_{gas}/M_{dust} vs. Z relation to derive M_{gas}, and under the assumption that the former does not evolve considerably with look back time. As pointed out in Magdis et al. (2012b) and in more detail by Berta et al. (2015), a critical component of this method relies on the existence of photometric data both at the peak of the far-IR SED but also in the R-J tail ($\lambda_{rest} > 250\,\mu$m). We note that this technique traces the total amount of neutral hydrogen in the ISM, thus $M_{gas} = M_{H_2} + M_{HI}$. However, based on observational evidence (e.g., Daddi et al. 2010a; Tacconi et al. 2010; Geach et al. 2011) as well as on theoretical arguments (Blitz & Rosolowsky 2006; Bigiel et al. 2008; Obreschkow & Rawlings 2009) we can assume that for our $z \sim 3$ galaxies, $M_{H_2} \gg M_{HI}$ or equivalently that $M_{gas} \approx M_{H_2}$.

Using the M_{dust} estimates from the DL07 models and assuming a solar metallicity for both sources we derive a gas mass of $\log(M_{H_2}\,[M_\odot]) = 11.12 \pm 0.25$ for D49 and $\log(M_{H_2}\,[M_\odot]) = 10.91 \pm 0.31$ for M28. Repeating the analysis based on metallicities derived from a broken FMR, would yield higher gas masses by a factor of 1.5 for both sources, that is 11.34 ± 0.25 for D49 and 11.12 ± 0.31 for M28.

4.2.3. $R - J$ based M_{H_2}

The available 1.2 mm data, that for the redshift of our sources correspond to $\lambda_{rest} \approx 300\,\mu$m, allows for a third estimate of M_{gas} that relies on single band measurement of the dust emission flux on the Rayleigh-Jeans side of the SED (e.g., Scoville et al. 2014, 2016). This technique converts the observed mm flux density into a cold gas mass, by making use of the observed relation between cold dust luminosity and gas mass in nearby galaxies.

Here we consider the calibration presented in Schinnerer et al. (2016), that was applied to a sample of $z \sim 3$ LBGs with available ALMA data in the R-J tail of the SED. Using the relations between monochromatic IR luminosities at 250, 350 and 500 μm and neutral gas mass from Groves et al. (2015) that are calibrated on observations for 36 local galaxies from the KINGFISH survey (Kennicutt et al. 2011), and adding a linear correction to the coefficients to account for the difference between observed and rest-frame wavelengths Schinnerer et al. (2016) provide the following formula:

$$\begin{aligned}\log(M_{gas}[M_\odot]) = {} & (1.57 - 8 \times 10^{-4}\Delta\lambda) \\ & + (0.86 + 6 \times 10^{-4}\Delta\lambda) \\ & \times \log(\nu L_\nu[L_\odot]), \end{aligned} \quad (5)$$

where

$$\Delta\lambda = \lambda_{rest} - 250\,\mu\text{m and } \nu L_\nu = \nu_{obs} \times S_{\nu,obs} \times 4\pi \times D_L^2. \quad (6)$$

Using the observed flux densities ($S_{\nu,obs}$) at 1.2 mm we infer (assuming again that $M_{gas} \approx M_{H_2}$) $\log(M_{H_2}\,[M_\odot]) = 11.29 \pm 0.31$ for D49 and $\log(M_{H_2}\,[M_\odot]) = 11.10 \pm 0.31$ for M28, in excellent agreement with the values derived based on the δ_{GD} approach. The limitations of this technique, that is not taking into account the evolution of the gas-phase metallicity and of the dust

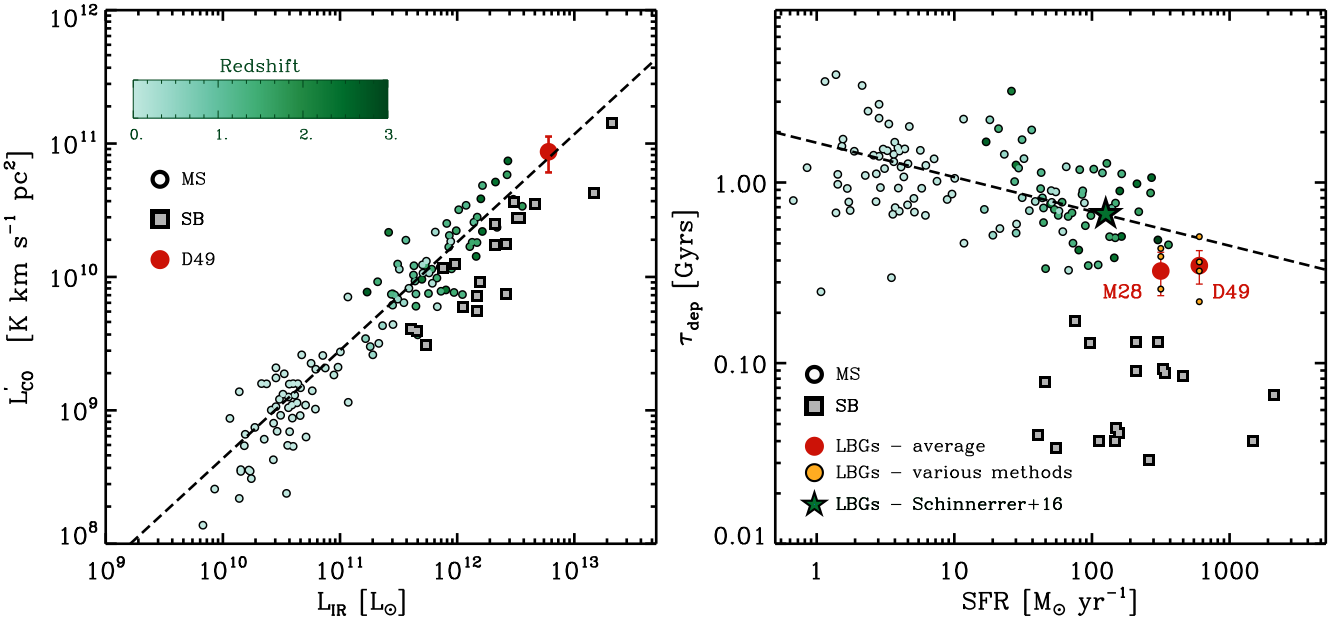

Fig. 6. *Left*: integrated Schmidt-Kennicutt relation using direct observables. Green circles correspond to MS galaxies, colour coded according to their redshift. Grey squares correspond to local and high-z star-bursts galaxies (×4 above the MS). The compilation of MS and SBs galaxies is presented in Sargent et al. (2014) and Silverman et al. (2016).The red dot depicts the position of D49, after converting the measured CO[$J = 3 \rightarrow 2$] luminosity to CO[$J = 1 \rightarrow 0$] assuming a line ratio of $r_{3,1} = 0.5$. The dashed line corresponds to the integrated Schmidt-Kennicutt relation of MS galaxies as derived by Sargent et al. (2014). *Right*: gas depletion time scale ($\tau_{dep} = M_{H_2}$/SFR or 1/SFE), based on the average M_{H_2} estimates from the various methods described in the text (filled red circles). The individual measurements based on various techniques and metallicity assumptions for each galaxy are depicted with orange circles. As in the left panel, literature MS galaxies are colour coded based on their redshift (see Sargent et al. 2014 for more details about the sample compilation). The dark green star corresponds to the average measurement reported by Schinnerer et al. (2016) for a sample of typical $z \sim 3.2$ LBGs, derived based on single mm band observations. The dashed line corresponds to the sequence of MS galaxies as derived by Sargent et al. (2014).

temperature of the galaxies (at fixed stellar mass) with redshift, are discussed in detail in Genzel et al. (2015), Berta et al. (2016) and Schinnerer et al. (2016). These limitations are more severe for the case of high-z star-bursting systems whose gas-phase metallicity could deviate much more than that of MS galaxies with respect to calibrations in the local universe. Thus, extra caution should be exercised when this technique is applied in high-z SB systems.

Comparing the M_{H_2} estimates from the various techniques we find an overall agreement within a factor of two or less, and M_{H_2} values that are consistent within the uncertainties linked wth each approach (Table 3).

4.3. Star formation law and SFE of z = 3 MS galaxies

Several studies have provided evidence that main sequence star-forming galaxies at all redshifts appear to follow a tight relation between their gas mass reservoir and their SFR, commonly referred to as the integrated Schmidt-Kennicutt relation. However, the sensitivity limits of *Herschel* and the time demanding nature of CO observations for MS galaxies, has largely restricted the measurement of the gas content of $z \sim 3$ MS galaxies to lensed objects or stacked ensembles (e.g., Saintonge et al. 2013), or more recently to M_{H_2} measurements based on a single band measurement of the dust emission flux on the Rayleigh-Jeans side of the SED (e.g. Scoville et al. 2014; Schinnerer et al. 2016). Indeed, direct CO detections of unlensed LBGs at $z > 3$ are restricted to two sources (e.g. Magdis et al. 2012a; Tan et al. 2014). Here, with three independent M_{H_2} measurements we are in position to investigate the star formation efficiency, defined by the ratio of the SFR over the molecular gas mass ($SFE = SFR/M_{H_2}$) of MS galaxies at $z \approx 3$.

Since $L_{IR} \propto SFR$ and $L'_{CO} \propto M_{H_2}$, this implies that $SFE \propto L_{IR}/L'_{CO}$. Therefore, it is useful to first consider the direct observables, L_{IR} and L'_{CO}, that are subject to fewer assumptions and uncertainties, before using the inferred SFRs and gas masses to investigate the SFE at $z \sim 3$. In Fig. 6 (left), we compare the CO and IR luminosity of D49, with other cosmologically relevant populations of MS and SB galaxies, drawn from the compilation presented in Sargent et al. (2014) along with data from Magdis et al. (2014) and Silverman et al. (2015). When required, higher transition CO luminosities (CO[$J = 2 \rightarrow 1$] and CO[$J = 3 \rightarrow 2$]), are converted to L'_{CO}, assuming typical excitation corrections ($r_{21} = 0.85$ and $r_{31} = 0.5$). It is clear that D49, follows the trend of local and high-z MS galaxies, as defined by Sargent et al. (2014) with a L_{IR}/L'_{CO} ratio of (71 ± 17) $L_\odot$/[K km s^{-1} pc^2]. While whether (a) SBs deviate from the L_{IR}–L'_{CO} relation of MS galaxies as a power-law to their offset from the MS (e.g. Tacconi et al. 2017; Scoville et al. 2017); or (b) there is a more abrupt transition between the MS and SB regime (2-SFM paradigm, Sargent et al. 2014), is still an open question, it is clear that SB galaxies have systematically larger L_{IR}/L'_{CO}ratios than MS galaxies. The average $\langle L_{IR}/L'_{CO} \rangle$ for SBs is 160 $L_\odot$/[K km s^{-1} pc^2], indicating a higher star formation efficiency with respect to D49 and other MS systems at various redshift by a factor of two or more, just by considering direct observables.

Using the derived SFR and M_{H_2} estimates of the two galaxies studied here, we then infer their gas depletion time scales defined as $\tau_{dep} = 1/SFE$. For each of the two galaxies, instead of choosing a single M_{H_2} measurement from one of the methods

Table 3. Molecular gas mass estimates.

Name	CO $\log(M_{H_2}/M_\odot)$	δ_{GD} $Z_\odot$ $\log(M_{H_2}/M_\odot)$	δ_{GD} "broken" FMR $\log(M_{H_2}/M_\odot)$	R-J $\log(M_{H_2}/M_\odot)$
D49	11.48 ± 0.23	11.12 ± 0.25	11.34 ± 0.25	11.29 ± 0.31
M28	–	10.91 ± 0.31	11.12 ± 0.31	11.10 ± 0.34

described above and summarised in Table 3, we adopt the average M_{H_2} as derived from all three (two) independent methods for D49 (M28). By combining the SFRs and the M_{H_2} of our galaxies, we find that both sources are characterised by very similar gas depletion time scales with $\tau_{dep} = (0.35 \pm 0.13)$ Gyr and $\tau_{dep} = (0.32 \pm 0.12)$ Gyr for D49 and M28 respectively. This is a factor of two lower compared to the average τ_{dep} found by Schinnerer et al. (2016) for a sample of less massive $z \sim 3$ LBGs. However, the τ_{dep} of our sources lie within the scatter of the $\tau_{dep} - SFR$ relation of Sargent et al. (2014) defined by MS galaxies across various cosmic epochs (Fig. 6, right).

Moving to gas-to-stellar mass ratios ($f_{gas} = M_{H_2}/M_*$), we find $f_{gas} = 1.1 \pm 0.2$ for D49 and 0.4 ± 0.1 for M28. Both values are consistent with previous studies that provide evidence for an increasing f_{gas} in MS galaxies with look-back time, that at $z > 2$ reaches a factor of ten with respect to local spirals (e.g. Magdis et al. 2012a,b; Geach et al. 2011; Tan et al. 2014). The factor of 2.5 difference in f_{gas} between the two galaxies in our sample should not come as surprise; apart from the expected intrinsic scatter, several studies have shown that f_{gas} among MS galaxies at a given redshift, increases as a power of the distance to the MS, $(sSFR/sSFR_{MS})^\gamma$ (e.g. Magdis et al. 2012b; Sargent et al. 2014; Genzel et al. 2015; Scoville et al. 2017). Adopting $\gamma = 0.8$ from Magdis et al. (2012b) and taking into account that D49 and M28 lie ×1.5 and ×1.4 above and below the MS respectively, suggests ∼×2 higher f_{gas} in D49 compared to M28. Thus, the observed difference in f_{gas} between the two galaxies is fully consistent with the notion of varying f_{gas} among MS galaxies at a given redshift. We note that we reach a similar conclusion when we consider a weaker dependance of f_{gas} on $sSFR/sSFR_{MS}$ ($\gamma \approx 0.3$–0.6) reported by other studies (e.g. Genzel et al. 2015; Scoville et al. 2017; Tacconi et al. 2017).

Put together, our analysis suggests that individual $z \sim 3$ MS galaxies appear to follow the SFR − M_{H_2} and $L_{IR} - L'_{CO}$ relations that are established at lower redshifts, indicating that overall MS framework holds at least up to $z \sim 3$.

5. Conclusions

Combining CO and dust measurements, we perform a detailed analysis of the dust and gas properties of two $z \sim 3$ MS galaxies. These are among a handfull of individually detected, unlensed, "normal" star-forming galaxies at $z > 2.5$ in the literature, with both CO detections and fully characterised IR SEDs out to the mm bands. Our findings can be summarised as follows:

- We confirm the increase of the mean radiation field $\langle U \rangle$ as a function of redshift, at least up to $z = 3$. This increase of $\langle U \rangle$ can be interpreted as a signature of an evolution toward lower gas-phase metallicities in $z > 2$ galaxies that is increased ("broken" FMR scenario in Sect. 4.1) with respect to expectations based on the universal FMR.
- For high-z MS galaxies, the various techniques to derive M_{H_2} provide consistent measurements, within a factor of two (or less). We note however, that this might not be the case for SBs, as their metallicity remains largely unconstrained.
- Our galaxies appear to follow the $L_{IR} - L'_{CO}$, $SFR - M_{H_2}$ relation established by "normal" galaxies at lower redshifts, extending the apparent uniformity of the star-forming galaxies out to $z = 3$.

Acknowledgements. This work is based on observations carried out under project number S14CN002, with the IRAM PdBI Interferometer. IRAM is supported by INSU/CNRS (France), MPG (Germany) and IGN (Spain). We are grateful to Prof. Alice Shapley for providing the UV spectrum of D49. G.E.M. acknowledges support from the Carlsberg Foundation, the ERC Consolidator Grant funding scheme (project ConTExt, grant number No. 648179), and a research grant (13160) from Villum Fonden. DR acknowledges support from ST/K00106X/1 and ST/N000919/1. C.F. acknowledges funding from the European Union's Horizon 2020 research and innovation programme under the Marie Sklodowska-Curie Grant agreement No 664931. MTS acknowledges support from a Royal Society Leverhulme Trust Senior Research Fellowship (LT150041). H.D. acknowledges financial support from the Spanish Ministry of Economy and Competitiveness (MINECO) under the 2014 Ramon y Cajal program MINECO RYC-2014-15686.

References

Amorín, R., Grazian, A., Castellano, M., et al. 2014, ApJ, 788, L4
Aravena, M., Spilker, J. S., Bethermin, M., et al. 2016, MNRAS, 457, 4406
Berta, S., Lutz, D., Genzel, R., Förster-Schreiber, N. M., & Tacconi, L. J. 2016, A&A, 587, A73
Béthermin, M., Daddi, E., Magdis, G., et al. 2015, A&A, 573, A113
Bigiel, F., Leroy, A., Walter, F., et al. 2008, AJ, 136, 2846
Blitz, L., & Rosolowsky, E. 2006, ApJ, 650, 933
Bothwell, M. S., Smail, I., Chapman, S. C., et al. 2013, MNRAS, 429, 3047
Carilli, C. L., & Walter, F. 2013, ARA&A, 51, 105
Chabrier, G. 2003, PASP, 115, 763
Ciesla, L., Boquien, M., Boselli, A., et al. 2014, A&A, 565, A128
Coppin, K. E. K., Geach, J. E., Almaini, O., et al. 2015, MNRAS, 446, 1293
Daddi, E., Dickinson, M., Morrison, G., et al. 2007, ApJ, 670, 156
Daddi, E., Elbaz, D., Walter, F., et al. 2010a, ApJ, 714, L118
Daddi, E., Bournaud, F., Walter, F., et al. 2010b, ApJ, 713, 686
Daddi, E., Dannerbauer, H., Liu, D., et al. 2015, A&A, 577, A46
Dannerbauer, H., Walter, F., & Morrison, G. 2009, ApJ, 698, L178
Dessauges-Zavadsky, M., Zamojski, M., Schaerer, D., et al. 2015, A&A, 577, A50
Donley, J. L., Koekemoer, A. M., Brusa, M., et al. 2012, ApJ, 748, 142
Elbaz, D., Daddi, E., Le Borgne, D., et al. 2007, A&A, 468, 33
Geach, J. E., Smail, I., Moran, S. M., et al. 2011, ApJ, 730, L19
Genzel, R., Tacconi, L. J., Combes, F., et al. 2012, ApJ, 746, 69
Genzel, R., Tacconi, L. J., Lutz, D., et al. 2015, ApJ, 800, 20
Greve, T. R., Leonidaki, I., Xilouris, E. M., et al. 2014, ApJ, 794, 142
Groves, B. A., Schinnerer, E., Leroy, A., et al. 2015, ApJ, 799, 96
Griffin, M. J., Abergel, A., Abreu, A., et al. 2010, A&A, 518, L3
Kreysa, E., Gemünd, H.-P., Gromke, J., et al. 1999, Infrared Physics & Technology, 40, 191
Lee, N., Sanders, D. B., Casey, C. M., et al. 2015, ApJ, 801, 80
Leroy, A. K., Bolatto, A., Gordon, K., et al. 2011, ApJ, 737, 12
Lilly, S. J., Carollo, C. M., Pipino, A., Renzini, A., & Peng, Y. 2013, ApJ, 772, 119
Lutz, D., Poglitsch, A., Altieri, B., et al. 2011, A&A, 532, A90
Magdis, G. E., Rigopoulou, D., Huang, J.-S., & Fazio, G. G. 2010a, MNRAS, 401, 1521
Magdis, G. E., Elbaz, D., Hwang, H. S., et al. 2010b, ApJ, 720, L185
Magdis, G. E., Elbaz, D., Daddi, E., et al. 2010c, ApJ, 714, 1740
Magdis, G. E., Daddi, E., Elbaz, D., et al. 2011, ApJ, 740, L15

Magdis, G. E., Daddi, E., Sargent, M., et al. 2012a, ApJ, 758, L9
Magdis, G. E., Daddi, E., Béthermin, M., et al. 2012b, ApJ, 760, 6
Magdis, G. E., Rigopoulou, D., Helou, G., et al. 2013, A&A, 558, A136
Magnelli, B., Lutz, D., Saintonge, A., et al. 2014, A&A, 561, A86
Mannucci, F., Cresci, G., Maiolino, R., Marconi, A., & Gnerucci, A. 2010, MNRAS, 408, 2115
Noeske, K. G., Weiner, B. J., Faber, S. M., et al. 2007, ApJ, 660, L43
Obreschkow, D., & Rawlings, S. 2009, ApJ, 696, L129
Oliver, S. J., Bock, J., Altieri, B., et al. 2012, MNRAS, 424, 1614
Peng, C. Y., Ho, L. C., Impey, C. D., & Rix, H.-W. 2002, AJ, 124, 266
Poglitsch, A., Waelkens, C., Geis, N., et al. 2010, A&A, 518, L2
Rigopoulou, D., Huang, J.-S., Papovich, C., et al. 2006, ApJ, 2006, 648, 81
Rigopoulou, D., Magdis, G., Ivison, R. J., et al. 2010, MNRAS, 409, L7
Saintonge, A., Lutz, D., Genzel, R., et al. 2013, ApJ, 778, 2
Santini, P., Maiolino, R., Magnelli, B., et al. 2014, A&A, 562, A30
Sargent, M. T., Daddi, E., Béthermin, M., et al. 2014, ApJ, 793, 19
Schreiber, C., Pannella, M., Elbaz, D., et al. 2015, A&A, 575, A74
Scoville, N., Aussel, H., Sheth, K., et al. 2014, ApJ, 783, 84
Scoville, N., Sheth, K., Aussel, H., et al. 2016, ApJ, 820, 83
Scoville, N., Lee, N., Vanden Bout, P., et al. 2017, ApJ, 837, 150
Shapley, A. E., Steidel, C. C., Pettini, M., & Adelberger, K. L. 2003, ApJ, 588, 65
Sharon, C. E., Riechers, D. A., Hodge, J., et al. 2016, ApJ, 827, 18
Schinnerer, E., Groves, B., Sargent, M. T., et al. 2016, ApJ, 833, 112
Silverman, J. D., Daddi, E., Rodighiero, G., et al. 2015, ApJ, 812, L23
Steidel, C. C., Adelberger, K. L., Shapley, A., et al. 2003, ApJ, 592, 728
Steidel, C. C., Rudie, G. C., Strom, A. L., et al. 2014, ApJ, 795, 165
Tacconi, L. J., Genzel, R., Neri, R., et al. 2010, Nature, 463, 781
Tacconi, L. J., Genzel, R., Saintonge, A., et al. 2017, ApJ, submitted [arXiv:1702.01140]
Tan, Q., Daddi, E., Magdis, G., et al. 2014, A&A, 569, A98
Troncoso, P., Maiolino, R., Sommariva, V., et al. 2014, A&A, 563, A58